Metal ion and ligand binding of integrin $\alpha_5\beta_1$

Wei Xia[a,b] and Timothy A. Springer[a,b,1]

[a]Program in Cellular and Molecular Medicine, Boston Children's Hospital, Boston, MA 02115; and [b]Department of Biological Chemistry and Molecular Pharmacology, Harvard Medical School, Boston, MA 02115

Contributed by Timothy A. Springer, October 30, 2014 (sent for review October 8, 2014)

Integrin $\alpha_5\beta_1$ binds to an Arg–Gly–Asp (RGD) motif in its ligand fibronectin. We report high-resolution crystal structures of a four-domain $\alpha_5\beta_1$ headpiece fragment, alone or with RGD peptides soaked into crystals, and RGD peptide affinity measurements. The headpiece crystallizes in a closed conformation essentially identical to that seen previously for $\alpha_5\beta_1$ complexed with a Fab that allosterically inhibits ligand binding by stabilizing the closed conformation. Soaking experiments show that binding of cyclic RGD peptide with 20-fold higher affinity than a linear RGD peptide induces conformational change in the β_1-subunit βI domain to a state that is intermediate between closed (low affinity) and open (high affinity). In contrast, binding of a linear RGD peptide induces no shape shifting. However, linear peptide binding induces shape shifting when Ca^{2+} is depleted during soaking. Ca^{2+} bound to the adjacent to metal ion-dependent adhesion site (ADMIDAS), at the locus of shape shifting, moves and decreases in occupancy, correlating with an increase in affinity for RGD measured when Ca^{2+} is depleted. The results directly demonstrate that Ca^{2+} binding to the ADMIDAS stabilizes integrins in the low-affinity, closed conformation. Comparisons in affinity between four-domain and six-domain headpiece constructs suggest that flexible integrin leg domains contribute to conformational equilibria. High-resolution views of the hybrid domain interface with the plexin–semaphorin–integrin (PSI) domain in different orientations show a ball-and-socket joint with a hybrid domain Arg side chain that rocks in a PSI domain socket lined with carbonyl oxygens.

Integrins are adhesion receptors that transmit bidirectional signals across the plasma membrane. The $\alpha_5\beta_1$ integrin and its primary extracellular matrix ligand fibronectin (Fn) are of great biological importance (1). Studies of this prototypic integrin–ligand pair led to the remarkable observation that much of the specific recognition by $\alpha_5\beta_1$ of the ∼2,000-residue fibronectin molecule was encoded by a 3-residue sequence, Arg–Gly–Asp (RGD), in Fn3 domain 10 (2). Eight of 24 integrin αβ heterodimers are now known to recognize RGD motifs within their ligands. Higher-affinity and more $\alpha_5\beta_1$-selective cyclic RGD peptide antagonists have been discovered (3) and mutationally characterized (4) but remain uncharacterized structurally.

Integrin αI and βI domains coordinate acidic residues in their ligands, such as the Asp side chain of RGD, through an Mg^{2+} ion held in a metal ion-dependent adhesion site (MIDAS) (5–8). βI domains also contain flanking Ca^{2+} ions coordinated by residues in the adjacent to MIDAS (ADMIDAS) and synergistic metal ion binding site (SyMBS). The ligand-binding headpiece of integrins has two states: a high-affinity, open conformation with the β-subunit hybrid domain swung out at its interface with the βI domain, and a low-affinity, closed conformation with the hybrid domain swung in (8). The altered conformation at the βI–hybrid domain interface is transmitted to an ∼3-Å rearrangement in the MIDAS- and ADMIDAS-coordinating βI domain β1-α1 loop, which alters affinity by ∼1,000-fold (9). The SyMBS and ADMIDAS have important roles in regulating ligand binding affinity (10, 11). The ADMIDAS is a negative regulatory site responsible for integrin inhibition by high concentration of Ca^{2+} and for activation by Mn^{2+}, which competes with Ca^{2+} for binding to the ADMIDAS (10, 11). However, the mechanism by which metals at the ADMIDAS regulate integrin affinity remains mysterious.

A recent structural study (12) revisited the role of Ca^{2+} at the ADMIDAS. The $\alpha_5\beta_1$ headpiece was characterized at 2.9-Å resolution bound to the SG/19 Fab that stabilizes the closed conformation of β_1 integrins by binding to the βI–hybrid domain interface. Soaking with RGD peptide induced movement of the βI domain β1-α1 loop and α1-helix, resulting in a conformational state intermediate between closed and open. A decrease in electron density for the ADMIDAS Ca^{2+} ion was also observed (12).

Here we report high-resolution crystal structures of the $\alpha_5\beta_1$ headpiece, alone or with soaked-in linear or cyclic peptides. Our results include important advances in understanding the role of Ca^{2+} binding to the ADMIDAS in ligand binding by β_1 integrins, how integrin $\alpha_5\beta_1$ binds cyclic peptides with high affinity, and the observation that Ca^{2+} at the ADMIDAS inhibits RGD-induced β1-α1 loop and α1-helix movement.

Results

Overall $\alpha_5\beta_1$ Headpiece Structure. We solved crystal structures at 1.78–2.5 Å (Table S1) of a four-domain fragment of the $\alpha_5\beta_1$ headpiece containing the α_5-subunit β-propeller domain and the β_1-subunit (Fig. S1) plexin–semaphorin–integrin (PSI), hybrid, and βI domains in a closed conformation (Fig. 1*A*). The orientation between the β_1-subunit βI and hybrid domains is very similar to that in the five-domain $\alpha_5\beta_1$ headpiece–SG/19 Fab complex (12) and in the closed $\alpha_{IIb}\beta_3$ conformation in the absence of ligand (13, 14), but is distinct from that in the open $\alpha_{IIb}\beta_3$ conformation found with crystallization in the presence of ligand (7) (Fig. 1*B*). The overall closed βI–hybrid domain orientation is supported by lattice contacts (Fig. S2), and is maintained in three RGD-soaked crystal structures.

SG/19 binds to the βI–hybrid domain interface and inhibits ligand binding allosterically by stabilizing this interface in its closed, low-affinity conformation (12, 15). SG/19 Fab buries 350 $Å^2$ of solvent-accessible surface on the βI domain (260 $Å^2$ of which is on the α1′-helix) and 790 $Å^2$ on the hybrid domain. The identical βI–hybrid domain orientation in the presence and absence of SG/19 Fab (Fig. 1*B*) agrees with the previous EM observation (15)

Significance

Three metal ions are at the heart of the ligand binding site in integrin β-subunits. Furthermore, motions at many domain–domain junctions in integrins regulate ligand binding affinity. High-resolution crystal structures and highly accurate solution ligand binding assays are required to understand the mechanisms by which integrins transmit conformational change in their complex dodecadomain ectodomains. Here we provide information fundamental to understanding these processes in the integrin that assembles fibronectin into fibrils in matrices, $\alpha_5\beta_1$.

Author contributions: W.X. and T.A.S. designed research; W.X. performed research; W.X. and T.A.S. analyzed data; and W.X. and T.A.S. wrote the paper.

The authors declare no conflict of interest.

Data deposition: The crystallography, atomic coordinates, and structure factors reported in this paper have been deposited in the Protein Data Bank, www.pdb.org (PDB ID codes 4WJK, 4WK0, 4WK2, and 4WK4).

[1]To whom correspondence should be addressed. Email: timothy.springer@childrens.harvard.edu.

This article contains supporting information online at www.pnas.org/lookup/suppl/doi:10.1073/pnas.1420645111/-/DCSupplemental.

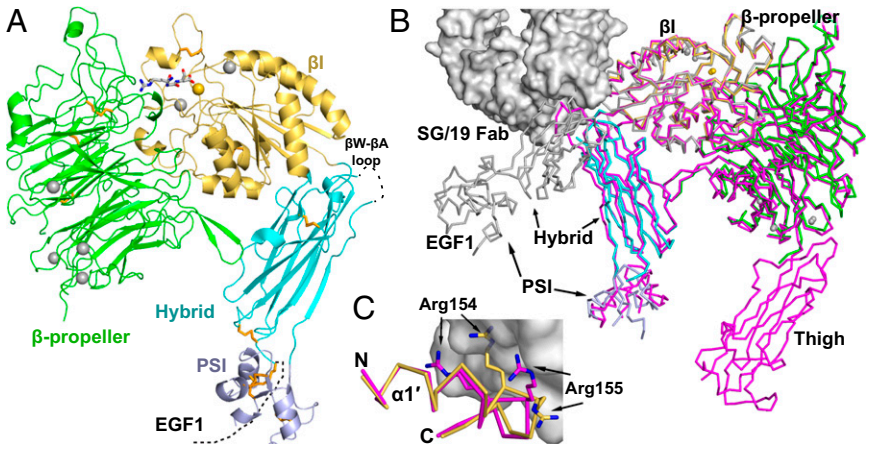

Fig. 1. Crystal structure of the $\alpha_5\beta_1$ integrin headpiece. (*A*) Ribbon diagram of $\alpha_5\beta_1$. The β-propeller, βI, hybrid, and PSI domains and RGD are in green, yellow orange, cyan, light blue, and gray, respectively. Ca^{2+} (silver) and Mg^{2+} (gold) are shown as spheres. Disulfide bonds (orange) and RGD are shown in stick representation. (*B*) Integrin headpiece comparisons. Four-domain $\alpha_5\beta_1$, color-coded as in *A*, five-domain $\alpha_5\beta_1$ (magenta) (12), and open $\alpha_{IIb}\beta_3$ (silver) (31) are superimposed and shown in Cα ribbon; for clarity, only β_3 of $\alpha_{IIb}\beta_3$ is shown. SG/19 Fab bound to five-domain $\alpha_5\beta_1$ (12) is shown as a surface. (*C*) Binding of SG/19 to the βI domain α1′-helix. Structures are colored and shown as in *B*, with the Arg-154 and -155 side chains also shown and the view rotated ∼180° around a vertical axis relative to *B*.

that SG/19 does not enforce an artificial orientation between the βI and hybrid domains but binds to the same overall closed hybrid–βI domain orientation as seen in the absence of Fab.

The closed conformation at the ligand binding site (Fig. 2), the α1-helix, and the N-terminal end of the α1′-helix are identical in the presence and absence of SG1/19 (Fig. 1*C*). However, SG/19 induces small conformational changes in its epitope. The hybrid domain βW-βA loop is flexible in the absence of SG/19: Our four-domain $\alpha_5\beta_1$ structures lack electron density for 5–8 residues at the tip of this loop. The loop becomes ordered when bound to SG/19 (Fig. 1*B*), and forms a substantial part of the epitope. SG/19 binds to the C-terminal end of the α1′-helix, a C-terminal continuation of the α1-helix (12). SG/19 slightly pushes α1′ inward to enable the α1′ Arg-154 and Arg-155 side chains to reorient and form part of the epitope (Fig. 1*C*).

Metal Ion and RGD Peptide Binding. $\alpha_5\beta_1$ crystals, formed in the presence of 1 mM Mg^{2+} and Ca^{2+} at pH 7.2, have excellent simulated-annealing omit map electron density for all three βI domain metal ions (Fig. 2*A*), as also seen with the $\alpha_5\beta_1$ complex with SG/19 crystallized at pH 6.5 (Fig. 2 *E* and *F*) (12).

Crystals soaked overnight with crystallization well solution containing 5 mM Mg^{2+}, 1 mM Ca^{2+}, and 10 mM GRGDSP peptide (corresponding to fibronectin residues 1523–1528) diffracted to 1.78-Å resolution (Table S1). RGD appeared in the ligand binding site with strong electron density. Complete occupancy (saturation binding) was confirmed by real space correlation coefficients (RSCCs) close to 1.0 (Table S2). The RGD Arg guanido group formed strong, bidentate, charged hydrogen bonds to α_5 Asp-227; in contrast, hydrogen bonding to α_5 Gln-221 was through two intermediate water molecules (Fig. 3*A*). The RGD Asp side chain coordinated the MIDAS Mg^{2+} ion using one oxygen and formed a weak, 3.4-Å hydrogen bond to the βI domain β1-α1 loop backbone through the other oxygen (Fig. 3*A*). RGD binding induced no movement in the β1-α1 loop or α1-helix, which were completely superimposable on the native (apo) structure (Fig. 4*A*), namely in closed "state 1" as defined by $\alpha_{IIb}\beta_3$ structures (9). Moreover, there was no loss of Ca^{2+} at the ADMIDAS; Ca^{2+} electron density after soaking with RGD peptide was as strong (Fig. 2*B*) as before (Fig. 2*A*) (Table S2).

To test the effect of omitting Ca^{2+}, we soaked crystals in crystallization solution containing 10 mM peptide, 5 mM Mg^{2+}, and no Ca^{2+}. The crystals diffracted to 2.5 Å and had excellent density for RGD (Fig. S3). In absence of added Ca^{2+}, RGD induced substantial movement of the β1-α1 loop and α1-helix (Fig. 4*B*), enabling the non–MIDAS-binding Asp carboxyl oxygen to form a stronger, 3.0-Å hydrogen bond to the β1-α1 loop backbone (Fig. 3*B*). Accompanying the movement of the β1-α1 loop, the side chain of Ser-134 moved to directly coordinate the MIDAS Mg^{2+} ion (Fig. 2*C*), displacing a water at the MIDAS seen with RGD in the presence of Ca^{2+} (Fig. 2*B*). Slight differences were also seen at the RGD Arg guanido group, which now formed a direct hydrogen bond to α_5 Gln-221 (Fig. 3*B*). Moreover, density for Ca^{2+} at the ADMIDAS was diminished, whereas there was little change in Ca^{2+} density at the SyMBS or Mg^{2+} density at the MIDAS (Fig. 2*C* compared with Fig. 2 *A* and *B*) (Table S2). These differences in the presence and absence of Ca^{2+} directly demonstrate that Ca^{2+} binding to the ADMIDAS inhibits RGD-induced shape shifting away from the closed conformation.

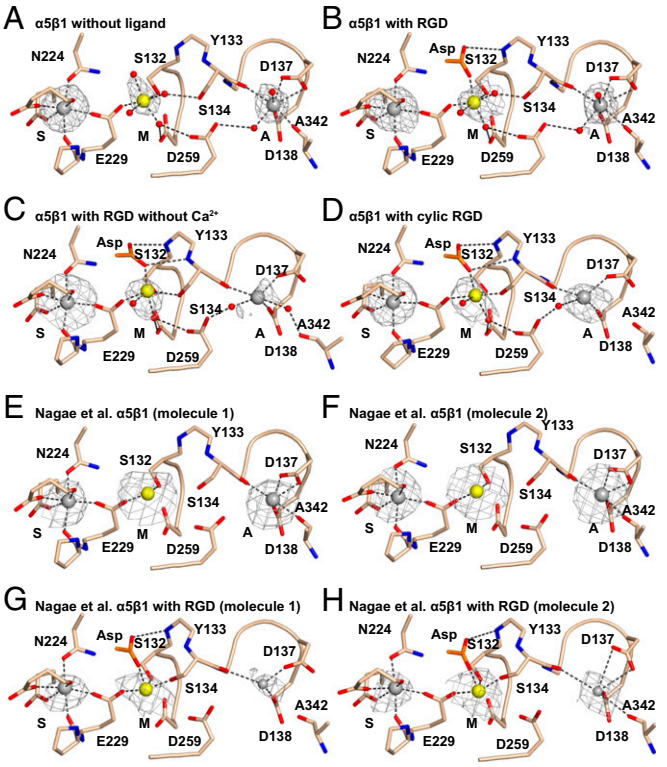

Fig. 2. βI domain metal binding sites. (*A–H*) The indicated structures are in identical orientations. Backbones and side chains of metal-coordinating residues are colored wheat with red oxygens and blue nitrogens. Waters are shown as small red spheres. Ca^{2+} (silver) and Mg^{2+} (gold) are shown as large spheres. Putative ADMIDAS Ca^{2+} ions not included in molecular models in *G* and *H* are shown as small spheres. Simulated-annealing omit map $F_o - F_c$ electron density contoured at 2.5σ is shown as mesh around metal ions.

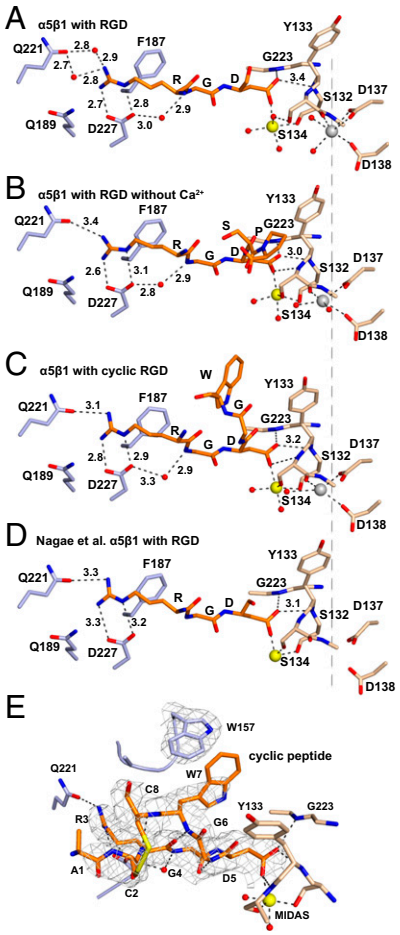

Fig. 3. RGD-binding pocket. (*A–D*) Vertical alignment in identical orientations with a dashed line for comparison. Residues of α_5 (light blue), β_1 (wheat), and ligand (RGD and two more C-terminal residues if built in the model) (orange) are shown in stick representation. Ca^{2+} (silver; ADMIDAS) and Mg^{2+} (gold; MIDAS) are shown as spheres. Waters are shown as small red spheres. Selected distances are shown in Å. (*E*) Binding of the cyclic peptide. The color scheme is as in *A–D*. All cyclic peptide residues visible in electron density are shown. $2F_o - F_c$ density at 1σ is shown as mesh for the cyclic peptide and α_5 Trp-157.

The intermediate state and diminishment of ADMIDAS Ca^{2+} electron density we observed when soaking with RGD peptide in the absence of Ca^{2+} were essentially identical to that obtained by Nagae et al. (12) when both Mg^{2+} and Ca^{2+} were omitted from the RGD soaking solution (Fig. 2*C* compared with Fig. 2 *G* and *H*, Fig. 3*B* compared with Fig. 3*D*, and Fig. 4*B* compared with Fig. 4*D*).

Complex with a Cyclic Peptide. The disulfide cyclized peptide ACRGDGWCG binds $\alpha_5\beta_1$ strongly and specifically (3, 4). A crystal soaked with 1 mM cyclic RGD peptide, 1 mM Mg^{2+}, and 1 mM Ca^{2+} in crystallization solution diffracted to 2.5 Å and showed strong density for the bound peptide (Fig. S3). Quite remarkably, binding of the cyclic peptide in the presence of Ca^{2+} induced shape shifting of the β1-α1 loop and α1 helix (Fig. 4*C*) similar to the linear peptide in the absence of Ca^{2+} (Fig. 4*B*). Furthermore, the cyclic peptide bound to $\alpha_5\beta_1$ (Fig. 3*C*) similar to the linear peptide in the absence of Ca^{2+} (Fig. 3*B*). The cyclic peptide also induced movement of the Ser-134 side chain into direct coordination with the MIDAS Mg^{2+} (Fig. 2*D*). Importantly, the ADMIDAS Ca^{2+} ion moved with the β1-α1 loop backbone (Fig. 4*C*) and with its Ser-134 carbonyl oxygen, which forms one ADMIDAS coordination (Fig. 2*D*). Also moving with the ADMIDAS Ca^{2+} ion was the α1-helix (Fig. 4*C*) with its Asp-137 and Asp-138 side chains, which form two further ADMIDAS coordinations (Fig. 2*D*). Moreover, electron density for the moved ADMIDAS Ca^{2+} was good (Fig. 2*D*), although weaker than the SyMBS Ca^{2+} electron density (Table S2). Shape shifting with (*i*) the cyclic peptide and Ca^{2+}, (*ii*) the linear peptide and Ca^{2+} depletion, and (*iii*) RGD in the SG/19 complex (12) was similar in extent to one another (Fig. 4 *B–D*), and approximated intermediate state 4 of $\alpha_{IIb}\beta_3$ (9).

The residues between the two disulfide-bonded cysteines in ACRGDGWCG were well-defined and show the basis for high-affinity binding (Fig. 3*E*). Cyclization decreases the conformational space accessible to a solvated peptide and thus lowers the entropic cost of becoming ordered when binding to a receptor. Moreover, the cyclic peptide conformation was stabilized by three backbone hydrogen bonds, including a 2.8-Å hydrogen bond with excellent geometry between the Arg-3 carboxyl oxygen and Trp-7 amide nitrogen. The cyclic peptide RGD moiety assumed a bound conformation very similar to that in linear RGD peptides (Fig. 3*C* compared with Fig. 3 *A*, *B*, and *D*). Importantly, the face of the cyclic peptide Trp side chain formed a T-shaped interaction with the edge of the α_5 Trp-157 side chain (Fig. 3*E* and Movie S1). T-shaped interactions are energetically favored by electrostatic interactions between the electron-rich edges and electron-poor centers of aromatic rings (16).

RGD Peptide Binding Affinity. Taking advantage of the relatively high affinity of the cyclic peptide, we labeled it fluorescently and measured affinity using the increase in fluorescence anisotropy upon binding to $\alpha_5\beta_1$ (17). The six-domain $\alpha_5\beta_1$ integrin headpiece fragment, containing thigh and EGF1 domains, bound with a K_D of 17.6 nM to the fluorescent cyclic peptide in 1 mM Mn^{2+}/0.1 mM Ca^{2+} (Fig. S4). Competitive binding showed a similar K_D of 22.6 nM for the unlabeled cyclic peptide (Fig. 5*A*). The linear GRGDSP peptide bound the six-domain headpiece with a markedly lower affinity, a K_D of 396 nM (Fig. 5*A*). Both cyclic and linear peptides exhibited twofold lower binding affinities to the four-domain integrin headpiece fragment lacking thigh and EGF1, with K_Ds of 43.7 nM and 862 nM, respectively (Fig. 5*B*). The affinity of cyclic RGD in 1 mM Mg^{2+}/1 mM Ca^{2+} was too low for accurate measurement using our method; however, the affinity for the six-domain $\alpha_5\beta_1$ headpiece in 5 mM Mg^{2+}/1 mM Ca^{2+}, the same conditions as used for GRGDSP soaking, was 1 μM (Fig. 5*C*). In contrast, the affinity in 5 mM Mg^{2+}, in the absence of Ca^{2+}, as also used in soaking, was 115 nM, and

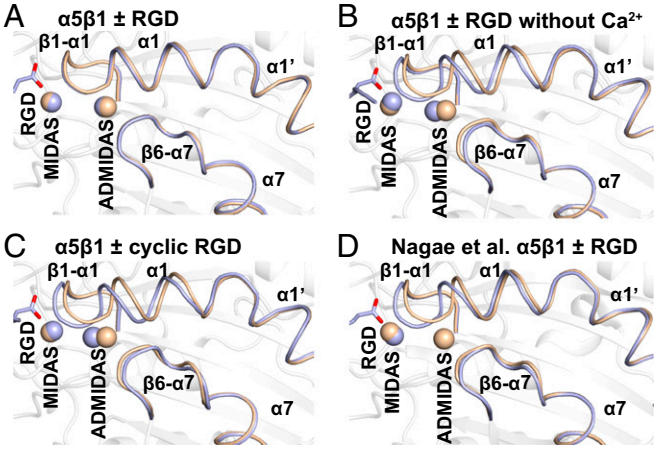

Fig. 4. RGD-induced conformational rearrangements in the βI domain. (*A–D*) The indicated unliganded (wheat) and RGD-soaked (light blue) structures are shown in identical orientations. Arg and Asp residues and disulfide bonds are shown in stick representation. Metals at MIDAS and ADMIDAS are shown as spheres.

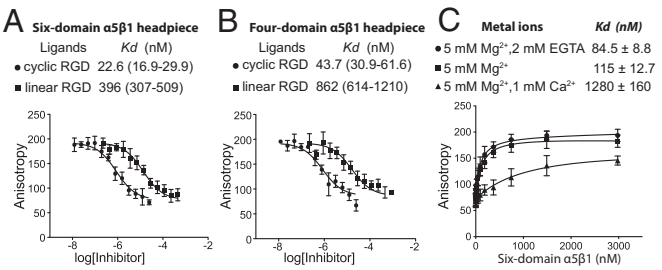

Fig. 5. RGD binding affinity. (*A* and *B*) Binding of six-domain $\alpha_5\beta_1$ (*A*) and four-domain $\alpha_5\beta_1$ (*B*) headpieces (200 nM) to linear and cyclic RGD peptides measured by competition with 2 nM fluorescent cyclic peptide using fluorescence anisotropy in 1 mM Mn^{2+} and 0.1 mM Ca^{2+}. (*C*) Binding of the six-domain $\alpha_5\beta_1$ headpiece to 2 nM fluorescent cyclic RGD peptide in different divalent cations. Data show mean ± SD of triplicate samples.

was 85 nM in 5 mM Mg^{2+}/2 mM EGTA. Thus, the β1-α1 loop and α1-helix movement seen with Ca^{2+} depletion correlated with about a 10-fold increase in $\alpha_5\beta_1$ affinity for ligand.

The Flexible Hybrid–PSI Interface. Among $\alpha_5\beta_1$ headpiece crystal structures, the orientation between hybrid and PSI domains varies by up to 15° (Fig. 1*B* and Table S3). Our two highest-resolution structures reveal the basis for flexibility at this interface (Fig. 6). The side chain of hybrid domain residue Arg-104 can rock and change rotamer while maintaining six or seven hydrogen bonds between its three guanido nitrogens and a socket in the PSI domain formed by carbonyl oxygens from the backbones of residues 19, 22, 23, 25, and 63 and the side chain of Asn-62 (Fig. 6).

Discussion

The resolution of the structures here surpasses previous limits of 2.35 Å for an open $\alpha_{IIb}\beta_3$ headpiece–RGD–Fab complex in Mn^{2+}/Ca^{2+} (9) and 2.2 Å for a closed $\alpha_{IIb}\beta_3$ headpiece–drug–Fab complex (18). Our 1.85-Å unliganded and 1.78- to 2.5-Å RGD-bound $\alpha_5\beta_1$ structures also represent improvements of 1.1–0.4 Å over previous 2.9-Å $\alpha_5\beta_1$ headpiece crystals (12). Deletion of the thigh domain in our four-domain $\alpha_5\beta_1$ headpiece compared with the previous five-domain headpiece (12) not only removed a flexible domain but also enabled formation of more compact crystals with 46% (vol/vol) solvent content (four-domain headpiece) compared with 61% solvent content (five-domain headpiece–Fab complex).

Headpiece structures provide insights into the flexibility of knee-proximal thigh, PSI, and EGF1 domains in the extended conformation of integrins. These domains show some flexibility in crystal structures of intact integrin ectodomains (19–22), in which the headpiece is bent at α-subunit thigh–calf-1 and β-subunit EGF1–EGF2 junctions and is in contact with the lower legs. Upper leg–lower leg interfaces and the closeness of the α-subunit and β-subunit knees help to stabilize the orientation of knee-proximal domains in the bent conformation. However, these constraints are removed upon integrin extension. PSI and EGF1 extend from the same end of the hybrid domain (Fig. 1 *A* and *B*). Interaction between PSI and EGF1 in β_2 integrins maintains similar hybrid–PSI and hybrid–EGF1 orientations in different $\alpha_x\beta_2$ ectodomain crystal forms and β_2 leg fragments (20, 21, 23, 24). In contrast, in $\alpha_4\beta_7$ headpiece 3.1-Å structures, both PSI and EGF1 domains were missing from electron density (25).

Electron density for the PSI domain is generally poorer than for other integrin domains in both bent ectodomain and headpiece structures. Although this is true in our structures as well, the overall higher-resolution (1.78 and 1.85 Å) $\alpha_5\beta_1$ headpiece structures show clear density at the hybrid–PSI interface and reveal the basis for flexibility. When the PSI domain moves relative to the hybrid domain, the side chain of hybrid domain residue Arg-104 rocks and changes rotamer to maintain an extensive network of hydrogen bonds to a socket in the PSI domain that is lined with backbone carbonyl oxygens. The presence of the hybrid domain Arg side chain in the PSI interface was previously described (7, 26), but not its role in PSI–hybrid reorientation. The Arg functions as a ball in a ball-and-socket joint between two tandem domains. We propose to call this motif a rocking Arg in a carbonyl socket. Perhaps the closest analogous interface is found in selectins between the lectin and EGF domains, where the α-amino group of the N-terminal Trp of the lectin domain pivots in an EGF domain carbonyl cage in selectin allostery (27).

Flexible domains or polypeptide segments distal from ligand binding interfaces may alter allosteric equilibria (28). We consistently found twofold higher ligand binding affinity of the six-domain than the four-domain $\alpha_5\beta_1$ headpiece for cyclic and linear RGD peptides. These differences cannot be accounted for by structural differences in the ligand-binding pocket. $\alpha_5\beta_1$ headpiece structures with (12) and without (here) the α-subunit thigh domain show no significant difference in the adjacent α-subunit β-propeller domain (0.29-Å rmsd over 402 Cα atoms). The thigh domain in integrins shows considerable flexibility at its interface with the β-propeller domain (20, 21, 25, 29). The hybrid, PSI, and EGF1 domains come much closer to the thigh domain in the closed than open headpiece conformation (Fig. 1*B*) and thus limit the range of orientations available to the thigh domain. Therefore, the presence of the thigh domain will entropically favor the open headpiece conformation. Similarly, the presence of the EGF1 domain in our six-domain but not four-domain headpiece will limit thigh domain flexibility in the closed conformation and favor the open headpiece conformation.

The cyclic peptide ACRGDGWCG was previously found to more effectively mediate and inhibit integrin $\alpha_5\beta_1$-dependent cell attachment to substrates than linear RGD peptides (3, 4). We found a 20-fold higher affinity of cyclic than linear RGD peptide for both four-domain and six-domain $\alpha_5\beta_1$ headpieces. This increase in affinity may be because cyclization together with backbone hydrogen bonds stabilizes a favorable conformation for binding to $\alpha_5\beta_1$ as shown in our structure. Alteration of the cyclic peptide Trp to Ala or mutation of α_5 Trp-157 to Ala greatly diminished cell attachment (4), successfully predicting the interaction of the peptide Trp with the α_5 Trp-157 visualized here. We see a T-shaped edge-to-center interaction known to stabilize aromatic interactions between the two Trp residues (16). Despite the importance of α_5 Trp-157 in binding the cyclic peptide, it is not important in binding fibronectin, which has a Pro residue in the equivalent position (4).

Our structures provide insights into how Ca^{2+} at the ADMIDAS regulates integrin affinity. Refinement in PHENIX (*Methods*) with different metal ions in our 1.78- and 1.85-Å structures

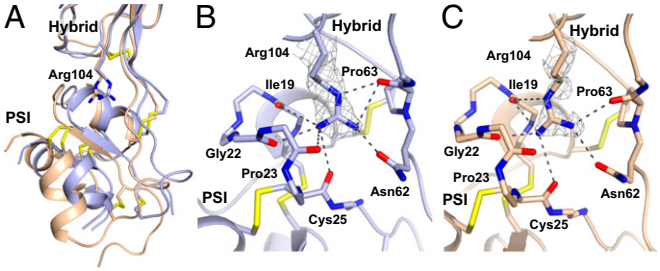

Fig. 6. Rocking at the hybrid–PSI interface. The change in PSI orientation is shown after superimposition on the hybrid domain. The rocking Arg-104 side chain in the hybrid domain shown in stick representation binds to a socket in PSI lined with carbonyl groups. Dashed lines indicate hydrogen bonds. (*A*) Combined view. (*B* and *C*) Individual detailed views, with $2F_o - F_c$ density for Arg-104 contoured at 1σ shown in mesh. Unliganded and linear RGD peptide + Ca^{2+} $\alpha_5\beta_1$ structures have carbons in light blue and wheat, respectively, and disulfide bonds in yellow.

strongly supports the assumption that in the closed conformation the SyMBS binds Ca^{2+}, the MIDAS binds Mg^{2+}, and the ADMIDAS binds Ca^{2+}. Importantly, when we compared the effect of soaking crystals with linear RGD peptide in the presence of Mg^{2+} and Ca^{2+} or in the presence of only Mg^{2+}, we found that RGD only induced β1-α1 loop and α1-helix movement toward the open conformation when Ca^{2+} was depleted. Furthermore, density for Ca^{2+} was diminished at the ADMIDAS but little affected at the SyMBS or the four β-propeller Ca^{2+}-binding hairpins (Table S2). These findings directly demonstrate that Ca^{2+} binding to the ADMIDAS stabilizes the closed conformation, and agree with our finding that Ca^{2+} depletion increases affinity for RGD peptide by 10-fold. We soaked crystals substantially longer (overnight) with RGD in the absence of Ca^{2+} than Nagae et al. (30 min) (12). However, the $t_{1/2}$ for diffusion of small ions such as Ca^{2+} into or out of ∼400-μm diameter protein crystals is only ∼20 s (30). In our RGD-soaked Ca^{2+}-depleted structure, we have placed Ca^{2+} at the ADMIDAS in the model, whereas Nagae et al. did not. However, RSCCs suggest in both cases a Ca^{2+} occupancy of 0.5–0.7 (Table S2).

Why in Ca^{2+} did the cyclic RGD peptide induce β1-α1 loop and α1-helix movement toward the open conformation whereas the linear peptide did not? Occupancy by RGD is essentially complete in both cases (Table S2). Thus, in contrast to our use of different concentrations of RGD to achieve different occupancies and different extents of opening in $\alpha_{IIb}\beta_3$ crystals (9), differing occupancy cannot explain the differences here. Three effects may be in play. (*i*) Although the bound conformations of RGD appear similar, there may be a significant difference in binding enthalpy to drive the shift. (*ii*) RGD slides slightly in its groove from β_1 toward α_5 between closed state 1 and intermediate state 4, as described for $\alpha_{IIb}\beta_3$ (9). Sliding is greater for cyclic RGD than linear RGD in state 4, particularly at the RGD Gly and Asp, and may be enhanced by the peptide Trp interaction with α_5 Trp-157, consistent with greater movement in this direction in the cyclic peptide of the backbone following the peptide Asp (Fig. 3*C* compared with Fig. 3*B*). (*iii*) In the linear peptide, the C-terminal Ser and Pro are disordered in the presence of Ca^{2+}, and have a spatial probability distribution that includes space that the side chain of Tyr-133 in the β1-α1 loop must occupy in intermediate state 4. This entropic barrier to β1-α1 loop shape shifting by the peptide C terminus is removed by cyclization. Notably, the peptide C terminus becomes ordered by the close approach of the β_1 Tyr-133 side chain in the Ca^{2+}-deficient complex (Fig. 3*B* compared with Fig. 3*A*), despite lower resolution compared with the Ca^{2+}-replete linear peptide complex.

Good density for the ADMIDAS Ca^{2+} in the intermediate state with the cyclic peptide shows that movement of ADMIDAS-coordinating residues does not abolish their interaction with Ca^{2+}; indeed, in our Ca^{2+}-depleted and -replete intermediate structures, as well as in models with Ca^{2+} added to the Nagae et al. structures, coordination to the Ser-134 backbone and Asp-137 and Asp-138 side chains is present in all cases (Fig. 2). However, we agree with the suggestion by Nagae et al. that breakage of the ADMIDAS coordination to the Ala-342 backbone in the β6-α7 loop, the first consequence of ADMIDAS movement, is associated with weaker ADMIDAS Ca^{2+} density. This is apparent from RSCCs with our cyclic RGD intermediate state, which shows an ADMIDAS Ca^{2+} occupancy of ∼0.6 (Table S2), and from the weaker density for the ADMIDAS metal ion in intermediate states 3–5 of $\alpha_{IIb}\beta_3$ (figure 2 in ref. 9).

According to the law of mass action, Ca^{2+} at the ADMIDAS can only favor the closed conformation over the open conformation if it is bound with higher affinity in the closed than open conformation. We have obtained the first structural correlate of this prediction, to our knowledge, by demonstrating that Ca^{2+} removal destabilizes the closed conformation and enables RGD to induce integrin movement toward the open state. Higher resolution than obtained here for the closed state in Mg^{2+}/Ca^{2+} (1.78 and 1.85 Å) or obtained for the open state in Mg^{2+}/Ca^{2+} (2.4 Å) (31) or in Mn^{2+}/Ca^{2+} (2.35 Å) (9) will be required for detailed analysis of metal ion coordination in the two states and to determine whether Mg^{2+} can replace Ca^{2+} at the ADMIDAS, as Mn^{2+} does (6, 9). At our current resolution it appears that the ADMIDAS Ca^{2+} coordination in the closed state is closest to pentagonal bipyramidal, with bidentate coordination in the closed state by the carboxyl oxygens of Asp-137 in the plane of the pentagon (Fig. 2 *A* and *B*). Whereas we see seven ADMIDAS Ca^{2+} coordinations in our 1.78- and 1.85-Å closed states (Fig. 2 *A* and *B*), we see only four or five ADMIDAS Ca^{2+} coordinations in the 2.5-Å intermediate-state structures (Fig. 2 *C* and *D*), correlating with lower Ca^{2+} occupancy. Furthermore, Asp-137 coordination is monodentate (Fig. 2 *C* and *D*). In open-conformation structures of $\alpha_{IIb}\beta_3$, coordination of Ca^{2+} or Mn^{2+} at the ADMIDAS is more octahedral, with monodentate coordination by the β_3 Asp corresponding to β_1 Asp-137 (9, 31). The open ADMIDAS coordination also differs from closed because ADMIDAS coordination by a β6-α7 loop backbone carbonyl is replaced by an Asp side chain that coordinates through a water to the MIDAS Mg^{2+} ion (7, 9). The preference of Ca^{2+} for pentagonal bipyramidal over octahedral coordination (32), together with changes in metal ligands between closed and open conformations, may explain why Ca^{2+} removal increases affinity for RGD and enables RGD to induce β1-α1 loop and α1-helix shape shifting. Conversely, Mg^{2+} and Mn^{2+} favor octahedral over pentagonal bipyramidal coordination (32), and their substitution for Ca^{2+} at the ADMIDAS may explain why Mn^{2+} and Mg^{2+}/EGTA (EGTA selectively chelates Ca^{2+}) are general activating agents for integrins (33, 34).

Our results are in excellent agreement with previous findings that Ca^{2+} exerts an inhibitory effect on β_1, β_2, and β_7 integrins by binding to the ADMIDAS (10, 11, 34, 35). However, the ideas expressed in the previous paragraph on how Mn^{2+} activates integrins are controversial, particularly for $\alpha_5\beta_1$, for which a large body of work has suggested that Mn^{2+} activates by binding to the MIDAS (10, 36). It is possible that Mn^{2+} activates $\alpha_5\beta_1$ by replacing both Mg^{2+} at the MIDAS and Ca^{2+} at the ADMIDAS; however, this fails to explain why, for most integrins, removal of Ca^{2+} by EGTA in the presence of excess Mg^{2+} activates as well as Mn^{2+}. An early $\alpha_v\beta_3$ crystal structure showed an intermediate RGD-bound state similar to that seen here, with separation between the MIDAS and ADMIDAS metal ions, and reported that in contrast to integrin αI domains, βI domains did not convert between open and closed states (6). $\alpha_5\beta_1$ mutational studies were therefore interpreted with the assumption that the MIDAS and ADMIDAS were independent of one another. However, we now know that integrin βI domains undergo opening to a high-affinity state, and that the ADMIDAS metal ion moves closer to the MIDAS metal ion. In the open state, the side chain of β_3 Asp-251, equivalent to β_1 Asp-259 (Fig. 2), forms a direct coordination to the ADMIDAS metal ion and an indirect coordination through a water to the MIDAS metal ion (7). Mutation of β_1 MIDAS residue Asp-130 abolishes the ability of Mn^{2+} to activate, but not the ability of Ca^{2+} to inhibit, binding of 12G10 antibody to an activation epitope on the βI domain α1′-helix involving residues Arg-154 and Arg-155 (36). In light of current structural knowledge, this suggests either that Mn^{2+} activates by binding to the MIDAS, or that Mn^{2+} activates at the ADMIDAS in a MIDAS-dependent manner, for example, that ADMIDAS movement into close proximity to the MIDAS with 12G10 epitope exposure requires a metal at the MIDAS. In further support for Mn^{2+} activation at the MIDAS, mutation of ADMIDAS residues Asp-138 and Asp-139 to Ala was found to still permit activation by Mn^{2+} and inhibition by Ca^{2+} (10). However, the D137A mutation lowered ligand binding affinity more than D138A, raising the possibility that D138A might not completely inhibit metal binding at the ADMIDAS; furthermore, ligand binding experiments showing stimulation by Mn^{2+} used the partially active D138A mutant and the stimulatory antibody 12G10, which might have acted like crutches to enable a crippled ADMIDAS to bind to Mn^{2+} when in its active,

MIDAS-proximal conformation. Integrins are perversely complicated, and a definitive understanding of how Mn^{2+} and Mg^{2+}/EGTA activate will require further work.

Methods

A six-domain $\alpha_5\beta_1$ headpiece containing α_5 residues F1–L609 and β_1 residues extending to the end of the EGF1 domain did not yield crystals, and its thigh domain resisted removal by proteolysis. Removal of thigh from $\alpha_{IIb}\beta_3$ by chymotrypsin is important in its crystallization (7). Therefore, we used a chimeric α-subunit constructed with the signal peptide and mature β-propeller residues F1–P450 of α_5 and thigh residues V453–D601 of α_{IIb}. The β_1-subunit was expressed with EGF1 (mature residues Q1–E481) or without EGF1 (Q1–E445). α_5 or α_5/α_{IIb} chimeric cDNAs were inserted into the XbaI and AgeI sites of pcDNA3.1/Hygro(-) vector, which contained a C-terminal tobacco etch virus (TEV) protease site, an acidic coiled-coil with a cysteine for disulfide-bond formation, and a Strep II tag (37). β_1 cDNAs were inserted into the BamHI and XbaI sites of pEF1-puro with a C-terminal TEV site, a basic coiled-coil with a cysteine, and a hexahistidine tag (37). HEK 293S *N*-acetylglucosaminyl transferase I–negative ($GnTI^{-/-}$) cells were cotransfected with the α_5 and EGF1-containing β_1 plasmids or the α_5/α_{IIb} chimera and EGF1-lacking β_1 plasmids and selected with 100 μg/mL hygromycin B and 3 μg/mL puromycin. Clones with high expression were cultured in EX-CELL 293 serum-free medium (Sigma-Aldrich) using shaking square bottles (38). Culture supernatant supplemented with 50 mM Tris·HCl (pH 8.0) and 300 mM NaCl was mixed with 40 mL of Ni-NTA Sepharose per liter. A column was washed with 20 mM Tris·HCl, 0.5 M NaCl, 10 mM imidazole (pH 8) and eluted with the same buffer with 300 mM imidazole. Eluted fractions were concentrated to ∼1 mg/mL in 20 mM Tris·HCl (pH 8.0), 150 mM NaCl (TBS) with 1 mM Mn^{2+}, 0.1 mM Ca^{2+}, 0.1 mM GRGDSP peptide and treated with 0.01 mg/mL α-chymotrypsin (crystallized and lyophilized; Sigma; C-4129) at 37 °C for 16 h to remove the thigh domain, C-terminal coiled-coil, and tags (Fig. S1). Protein was further purified and separated from GRGDSP peptide by Superdex 200 size-exclusion chromatography in TBS with 1 mM Mg^{2+} and 1 mM Ca^{2+} to produce the four-domain (β-propeller, PSI, hybrid, and βI) construct. A six-domain $\alpha_5\beta_1$ headpiece construct (β-propeller, thigh, PSI, hybrid, βI, and EGF1) was expressed and purified identically, except TEV protease was used to remove the C-terminal coiled-coil and tags.

The four-domain $\alpha_5\beta_1$ integrin headpiece was concentrated to 5 mg/mL in TBS, 1 mM Mg^{2+}, and 1 mM Ca^{2+} and initially crystalized at 20 °C in 0.1 M Hepes (pH 6.5), 20% PEG 6000 using hanging-drop vapor diffusion. Diffraction-quality single crystals were obtained in 0.1 M Hepes (pH 7.2), 16% PEG 6000 with microseeding. For soaking overnight, single crystals were transferred to well solution supplemented with the indicated concentrations of peptides and metal ions (Table S1). Finally, crystals were transferred to well solution supplemented with 15% ethylene glycol with about 30 s at each of three 5% steps and frozen in liquid nitrogen. Diffraction data were processed with XDS (39). Structures were solved by molecular replacement. The apo structure was solved with the $\alpha_5\beta_1$ structure [Protein Data Bank (PDB) ID code 3VI3] and the refined apo structure was used as the search model for RGD complexes. Models were built with Coot (40) and refined with PHENIX (41). Simulated-annealing omit and composite omit maps and RSCCs were calculated with PHENIX.

Cyclic and linear RGD peptides (>95% pure) were synthesized by GenScript. The cyclic RGD peptide was made fluorescent by synthesizing it with fluorescein isothiocyanate and 6-aminohexanoic acid linked to its N terminus.

All saturation and competition fluorescence anisotropy was performed in 20 mM Tris buffer (pH 7.4), 150 mM NaCl supplemented with the indicated metal ions and 2 nM fluorescent cyclic RGD. Binding affinities were calculated as described (17). In saturation binding assays, anisotropy was measured with the six-domain or four-domain $\alpha_5\beta_1$ (starting at 500 nM) serially diluted in twofold decrements. Competition assays contained 200 nM $\alpha_5\beta_1$, 2 nM fluorescent probe, and twofold serially diluted competing peptide.

ACKNOWLEDGMENTS. We thank beamline 24ID at the Advanced Photon Source and Jianghai Zhu, Xianchi Dong, and Li-Zhi Mi for help with data collection and refinement. Supported by NIH Grant HL-108248.

1. Schwarzbauer JE, DeSimone DW (2011) Fibronectins, their fibrillogenesis, and in vivo functions. *Cold Spring Harb Perspect Biol* 3(7):1–19.
2. Pierschbacher MD, Ruoslahti E (1984) Cell attachment activity of fibronectin can be duplicated by small synthetic fragments of the molecule. *Nature* 309(5963):30–33.
3. Koivunen E, Wang B, Ruoslahti E (1995) Phage libraries displaying cyclic peptides with different ring sizes: Ligand specificities of the RGD-directed integrins. *Biotechnology (N Y)* 13(3):265–270.
4. Humphries JD, et al. (2000) Molecular basis of ligand recognition by integrin α5β1. II. Specificity of Arg-Gly-Asp binding is determined by Trp157 of the α subunit. *J Biol Chem* 275(27):20337–20345.
5. Lee J-O, Rieu P, Arnaout MA, Liddington R (1995) Crystal structure of the A domain from the α subunit of integrin CR3 (CD11b/CD18). *Cell* 80(4):631–638.
6. Xiong JP, et al. (2002) Crystal structure of the extracellular segment of integrin α Vbeta3 in complex with an Arg-Gly-Asp ligand. *Science* 296(5565):151–155.
7. Xiao T, Takagi J, Coller BS, Wang JH, Springer TA (2004) Structural basis for allostery in integrins and binding to fibrinogen-mimetic therapeutics. *Nature* 432(7013):59–67.
8. Springer TA, Dustin ML (2012) Integrin inside-out signaling and the immunological synapse. *Curr Opin Cell Biol* 24(1):107–115.
9. Zhu J, Zhu J, Springer TA (2013) Complete integrin headpiece opening in eight steps. *J Cell Biol* 201(7):1053–1068.
10. Mould AP, Barton SJ, Askari JA, Craig SE, Humphries MJ (2003) Role of ADMIDAS cation-binding site in ligand recognition by integrin α5β1. *J Biol Chem* 278(51): 51622–51629.
11. Chen J, Salas A, Springer TA (2003) Bistable regulation of integrin adhesiveness by a bipolar metal ion cluster. *Nat Struct Biol* 10(12):995–1001.
12. Nagae M, et al. (2012) Crystal structure of α5β1 integrin ectodomain: Atomic details of the fibronectin receptor. *J Cell Biol* 197(1):131–140.
13. Zhu J, et al. (2009) The structure of a receptor with two associating transmembrane domains on the cell surface: Integrin αIIbβ3. *Mol Cell* 34(2):234–249.
14. Zhu J, et al. (2010) Closed headpiece of integrin αIIbβ3 and its complex with an αIIbβ3-specific antagonist that does not induce opening. *Blood* 116(23):5050–5059.
15. Luo B-H, Strokovich K, Walz T, Springer TA, Takagi J (2004) Allosteric β1 integrin antibodies that stabilize the low affinity state by preventing the swing-out of the hybrid domain. *J Biol Chem* 279(26):27466–27471.
16. Burley SK, Petsko GA (1985) Aromatic-aromatic interaction: A mechanism of protein structure stabilization. *Science* 229(4708):23–28.
17. Rossi AM, Taylor CW (2011) Analysis of protein-ligand interactions by fluorescence polarization. *Nat Protoc* 6(3):365–387.
18. Zhu J, et al. (2012) Structure-guided design of a high-affinity platelet integrin αIIbβ3 receptor antagonist that disrupts Mg^{2+} binding to the MIDAS. *Sci Transl Med* 4(125): 125ra132.
19. Dong X, et al. (2012) αVβ3 integrin crystal structures and their functional implications. *Biochemistry* 51(44):8814–8828.
20. Sen M, Yuki K, Springer TA (2013) An internal ligand-bound, metastable state of a leukocyte integrin, αXβ2. *J Cell Biol* 203(4):629–642.
21. Xie C, et al. (2010) Structure of an integrin with an αI domain, complement receptor type 4. *EMBO J* 29(3):666–679.
22. Zhu J, et al. (2008) Structure of a complete integrin ectodomain in a physiologic resting state and activation and deactivation by applied forces. *Mol Cell* 32(6): 849–861.
23. Shi M, et al. (2007) A structural hypothesis for the transition between bent and extended conformations of the leukocyte β2 integrins. *J Biol Chem* 282(41): 30198–30206.
24. Shi M, et al. (2005) The crystal structure of the plexin-semaphorin-integrin domain/hybrid domain/I-EGF1 segment from the human integrin β2 subunit at 1.8-Å resolution. *J Biol Chem* 280(34):30586–30593.
25. Yu Y, et al. (2012) Structural specializations of α4β7 an integrin that mediates rolling adhesion. *J Cell Biol* 196(1):131–146.
26. Xiong JP, Stehle T, Goodman SL, Arnaout MA (2004) A novel adaptation of the integrin PSI domain revealed from its crystal structure. *J Biol Chem* 279(39):40252–40254.
27. Springer TA (2009) Structural basis for selectin mechanochemistry. *Proc Natl Acad Sci USA* 106(1):91–96.
28. Motlagh HN, Wrabl JO, Li J, Hilser VJ (2014) The ensemble nature of allostery. *Nature* 508(7496):331–339.
29. Yu Y, Schürpf T, Springer TA (2013) How natalizumab binds and antagonizes α4 integrins. *J Biol Chem* 288(45):32314–32325.
30. Geremia S, Campagnolo M, Demitri N, Johnson LN (2006) Simulation of diffusion time of small molecules in protein crystals. *Structure* 14(3):393–400.
31. Springer TA, Zhu J, Xiao T (2008) Structural basis for distinctive recognition of fibrinogen γC peptide by the platelet integrin αIIbβ3. *J Cell Biol* 182(4):791–800.
32. Harding MM (2001) Geometry of metal-ligand interactions in proteins. *Acta Crystallogr D Biol Crystallogr* 57(Pt 3):401–411.
33. Gailit J, Ruoslahti E (1988) Regulation of the fibronectin receptor affinity by divalent cations. *J Biol Chem* 263(26):12927–12932.
34. Dransfield I, Cabañas C, Craig A, Hogg N (1992) Divalent cation regulation of the function of the leukocyte integrin LFA-1. *J Cell Biol* 116(1):219–226.
35. Kamata T, et al. (2002) The role of the CPNKEKEC sequence in the β2 subunit I domain in regulation of integrin αLβ2. *J Immunol* 168(5):2296–2301.
36. Mould AP, et al. (2002) Integrin activation involves a conformational change in the α1 helix of the β subunit A-domain. *J Biol Chem* 277(22):19800–19805.
37. Nishida N, et al. (2006) Activation of leukocyte β_2 integrins by conversion from bent to extended conformations. *Immunity* 25(4):583–594.
38. Muller N, Girard P, Hacker DL, Jordan M, Wurm FM (2005) Orbital shaker technology for the cultivation of mammalian cells in suspension. *Biotechnol Bioeng* 89(4):400–406.
39. Kabsch W (1993) Automatic processing of rotation diffraction data from crystals of initially unknown symmetry and cell constants. *J Appl Crystallogr* 26(Pt 6):795–800.
40. Emsley P, Cowtan K (2004) Coot: Model-building tools for molecular graphics. *Acta Crystallogr D Biol Crystallogr* 60(Pt 12 Pt 1):2126–2132.
41. Adams PD, et al. (2010) PHENIX: A comprehensive Python-based system for macromolecular structure solution. *Acta Crystallogr D Biol Crystallogr* 66(Pt 2):213–221.